

Unconventional superconducting gap via spin fluctuations in iron-vacancy ordered $A_y\text{Fe}_{2-x}\text{Se}_2$

Shin-Ming Huang¹ and Chung-Yu Mou^{1,2,3}

¹*Department of Physics, National Tsing Hua University, Hsinchu 30043, Taiwan*

²*Institute of Physics, Academia Sinica, Nankang, Taiwan and*

³*Physics Division, National Center for Theoretical Sciences, P.O.Box 2-131, Hsinchu, Taiwan*

Based on an effective 12-orbital tight-binding model, we examine the superconducting states induced by the antiferromagnetic fluctuations for iron-vacancy-ordered $A_y\text{Fe}_{2-x}\text{Se}_2$. It is shown that due to the broken reflection symmetry induced by the iron vacancies, new superconducting states with C_{4h} symmetry emerge. In particular, we show that in the C_{4h} symmetry, symmetric axes of the pairing momenta do not need to coincide with axes of the unit cell. As a result, in addition to the magnitude of the pairing gap, the relative orientation of the pairing wave function to the lattice forms another degree of freedom for characterizing the superconducting gap and can further help in gaining the condensation energy. Nonetheless, similar to other iron-based superconductors, the singlet ground state is still dominated by s -wave or d -wave, which are nearly degenerate with anisotropic gaps. Furthermore, s -wave and d -wave superconducting states are separated by a quantum critical point controlled by the Hund's rule coupling J_H .

PACS numbers: 74.70.Xa, 74.20.Mn, 74.20.Rp

I. INTRODUCTION

Since the discovery of high-temperature superconductivity in cuprates, it has been a key interest to find the mechanism that causes the high T_c and its unconventional nature. After more than 20 years of intensive investigations, however, the origin of high- T_c superconductivity in cuprates is still unsolved. The discovery of relatively high T_c in iron-based superconductors^{1,2} opens a different route for high-temperature superconductivity and thus provides a unique opportunity to re-clarify the physics of the unconventional superconductivity. One of the features for the unconventional superconductivity is the appearance of the sign-switched gap function. The presence of disconnected Fermi surface (FS) sheets in iron-based superconductors is an ingenious condition for the existence of the sign-switched order parameters such as s_{\pm} -wave and d -wave³. It is widely believed that the superconducting (SC) pairing is driven by the inter-FS-sheet scattering or equivalently by the antiferromagnetic (AFM) fluctuations⁴⁻⁶ as the inter-FS-sheet scattering also leads to a strong AFM correlation.

The recent discovery of alkaline-intercalated iron-selenide superconductor $A_y\text{Fe}_{2-x}\text{Se}_2$ with T_c above 30K⁷ initiates an interesting branch for exploring superconductivity in iron-based superconductors. The chemically-stable structure $A_{0.8}\text{Fe}_{1.6}\text{Se}_2$ exhibits a $\sqrt{5} \times \sqrt{5}$ iron-vacancy order and block-checkerboard antiferromagnetism⁸⁻¹⁰. By varying contents of iron or alkaline, the AFM state becomes unstable and the SC state appears^{11,12}. More recently, it is indicated that the antiferromagnetic phase and the superconducting phase may be separated in different space regions¹³⁻¹⁸. In particular, a scanning tunneling microscopy (STM) measurement¹⁹ shows that the sample would be spontaneously separated into the superconducting KFe_2Se_2 and the insulating $\text{K}_x\text{Fe}_{1.6}\text{Se}_2$. Nevertheless, it still

needs further clarification to see if the insulating region can be altered into a metal by chemical doping or by applying pressure. First-principles calculations indicate that by applying pressure to samples with the $\sqrt{5} \times \sqrt{5}$ iron-vacancy order, the system goes through two successive magnetic transitions, from the semiconducting block-checkerboard AFM phase to the metallic stripe (collinear) AFM phase and then to a metallic non-magnetic phase²⁰. These results agree with transport measurements and indicate that a semiconductor-to-metal transition can be induced by the pressure²¹. The issue of whether the iron-vacancy-ordered $A_y\text{Fe}_{2-x}\text{Se}_2$ supports superconductivity, however, remains unsettled as it is shown that as the system became more metallic under pressure, T_c gets smaller, and whether it suggests the necessity of strong correlation for the emergence of superconductivity is an open question.

On the other hand, nuclear magnetic resonance (NMR) experiments find singlet superconductivity and no pronounced spin fluctuations near T_c ²³⁻²⁵. The spin-lattice relaxation rate $1/T_1T$ shows the absence of the Hebel-Slichter coherence peak and a power-law behavior below T_c , indicating an unconventional SC gap which is very likely gapless. Although salient spin fluctuations are not present in NMR, the possibility of spin-fluctuation-driven superconductivity should not be excluded since the formation of spin fluctuations would be hidden in signals²⁶. A recent Raman measurement on the two-magnon scattering shows that the scattering rate grows as the temperature approaches T_c and undergoes a sudden drop when the system enters the SC phase²⁷. It thus supports that superconductivity arises from magnetic fluctuations.

Theoretically, previous works²⁸⁻³³ on superconductivity in $A_y\text{Fe}_{2-x}\text{Se}_2$ were based on the band structure of KFe_2Se_2 ^{34,35}. However, the iron-vacancy order has been proved to induce a big change in the FS shape^{10,36}, though it is not confirmed so far by the angle-resolved

photoemission spectroscopy (ARPES)^{37–40}. Therefore, if superconductivity could happen in the iron-vacancy ordering phase, it is crucial to examine the pairing symmetry and pairing mechanism.

In this work, we investigate superconducting instability in iron-vacancy-ordered $A_yFe_{2-x}Se_2$. Previously, based on the 12-orbital tight-binding model that fits the band structure of $K_yFe_{2-x}Se_2$, we have studied the magnetic phase in the generalized Hubbard model and succeeded in explaining the block-checkerboard AFM instability from the Stoner's theory⁴¹. Here based on the same tight-binding model and starting from a non-magnetic metallic phase, we examine the superconductivity by the fluctuation-exchange (FLEX) approach^{42,43}. For singlet superconductivity, we examine the pairing coupling constants for s -wave and d -wave states from the effective scattering matrix. We find that similar to other iron-pnictide superconductors⁶, s -wave and d -wave are closely degenerate. Furthermore, the gap functions in both symmetries are highly anisotropic and have nodes. In addition, since the iron-vacancy order lowers the symmetry of $A_yFe_{2-x}Se_2$ to the group C_{4h} , the gap functions do not need to be reflection symmetric and this implies that there are degrees of freedom in defining origins of angles for the pairing momenta. These extra degrees of freedom for the gap functions can further increase the gain of the condensation energy. In addition, we find that the pairing symmetry is controllable by tuning the Hund's rule coupling J_H and the critical value at about $J_H = 0.2U$. The Hund's rule coupling manipulates the phase transition or crossover in superconductivity, antiferromagnetism⁴¹, or even the metallic transport⁴⁵, reflecting the substantial role played by the orbital-correlation in the multi-orbital electronic systems.

II. THEORETICAL METHOD

The vacancy ordered iron selenide $A_yFe_{2-x}Se_2$ is a system with one-fifth of Fe being taken off and forming a characteristic $\sqrt{5} \times \sqrt{5}$ pattern (Fig. 1(a)). The presence of the iron vacancy changes the space group from I_4/mmm (D_{4h}) to I_4/m (C_{4h}). As a result, the four-fold rotational symmetry is retained without the reflection symmetry with respect to the xz , yz and the diagonal planes. The absence of reflection symmetry implies that there is no symmetry axis. Hence there is an extra degree of freedom in defining the zero value of angles for basis functions of C_{4h} . For instance, the basis function $\cos(4\theta)$ becomes $\cos[4(\theta - \theta_0)]$ with θ_0 being a free parameter.

To implement the I_4/m symmetry for $A_yFe_{2-x}Se_2$, we have constructed a 12-orbital tight-binding model with four Fe atoms (labeled by A , B , C , and D) per cell and three t_{2g} orbitals (d_{xz} , d_{yz} , and d_{xy} with x and y referring to Fe-Fe directions) per Fe to investigate the magnetic instability⁴¹. The resulting FS is shown in Fig. 1(b) with two hole pockets, α_1 the one centering on $(0,0)$ and α_2 on (π,π) , and four electron pockets, β_1 the one and its in-

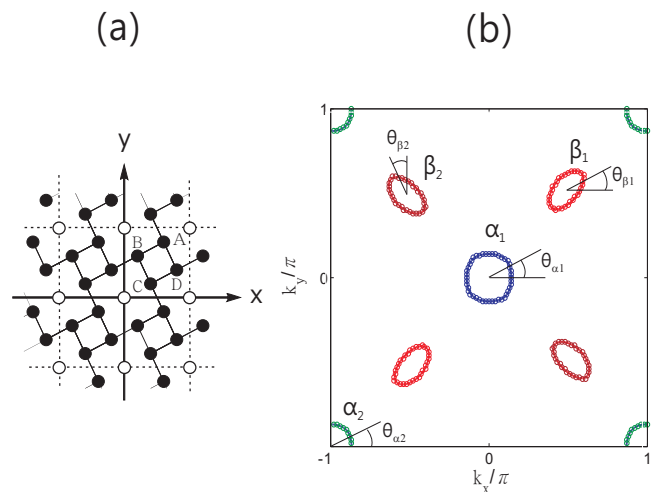


FIG. 1: (Color online) (a) The illustration of the Fe plane with the left chiral $\sqrt{5} \times \sqrt{5}$ vacancy ordering. The solid circles denote Fe atoms and the empty ones the vacancies. Every four nearest vacancies enclose the unit cells. Each unit cell contains four Fe atoms, labeled by A , B , C , and D . x and y are the primitive vectors. (b) The Fermi surface results from the 12-orbital tight-binding model: two hole pockets (α_1 and α_2) and four electron pockets (β_1 and β_2 and their inverse partners). 216 k -points on the Fermi surfaces are selected and shown by circles (zoom in to see). Points on FS- α_1 , α_2 , β_1 and β_2 are parameterized by the angles, θ_{α_1} , θ_{α_2} , θ_{β_1} , and θ_{β_2} , respectively.

version around $\pm(\pi/2, \pi/2)$ and β_2 around $\pm(-\pi/2, \pi/2)$. To calculate the SC gap, we shall divide the momentum k space into a lattice with 200×200 points and approximate states on the FS sheets by picking totally 216 k points with 44 points on FS- α_1 , 40 points on FS- α_2 , and 66 points both on FS- β_1 and β_2 . These k points on FS sheets are characterized by angles, θ_{α_1} , θ_{α_2} , θ_{β_1} , and θ_{β_2} as illustrated in Fig. 1(b). All angles are relative to the horizontal k_x axis except that θ_{β_2} is relative to the vertical k_y axis due to that FS- β_2 is a 90° rotation from FS- β_1 . On the average, the energy resolution in the \mathbf{k} space with 200×200 points within a 50meV window relative to the Fermi energy is 0.6meV, while for the chosen 216 k points, the momentum resolution is about $\Delta k = \pi/100$ and we estimate the corresponding energy resolution is about 4meV.

We shall assume that the interaction between electrons on each Fe atom is given by the generalized Hubbard model,

$$\begin{aligned}
 H_I = & \sum_i \sum_I \left\{ U \sum_{a=1}^3 n_{aI,i\uparrow} n_{aI,i\downarrow} \right. \\
 & + \sum_{a,b(a>b)} \left[\left(U' - \frac{J_H}{2} \right) n_{aI,i} n_{bI,i} - 2J_H \mathbf{S}_{aI,i} \cdot \mathbf{S}_{bI,i} \right. \\
 & \left. \left. + J_C \left(d_{aI,i\uparrow}^\dagger d_{aI,i\downarrow}^\dagger d_{bI,i\downarrow} d_{bI,i\uparrow} + h.c. \right) \right] \right\}, \quad (1)
 \end{aligned}$$

where I is the index for four Fe atoms and a is the index for three t_{2g} orbitals. It was found⁴¹ that as the interaction turns on, the spin fluctuation is strong at $\mathbf{q} = (\pi, \pi)$ and $(\pi, 0)$, in which the former is related to the checkerboard antiferromagnetism and the latter is related to the stripe antiferromagnetism. These two magnetic states competes each other and the preference between them is controlled by the Hund's rule coupling, J_H .

The strong spin fluctuation is a possible pairing mechanism. To investigate the superconductivity arising from the exchange of spin and charge fluctuations, we follow the FLEX approach^{42,43}, in which the effective singlet pairing scattering matrix is given by

$$\Gamma_{cd}^{ab}(\mathbf{k}, \mathbf{k}'; \omega) = \left[\frac{3}{2} \Gamma_s \chi_{RPA}^s(\mathbf{k} - \mathbf{k}', \omega) \Gamma_s + \frac{1}{2} \Gamma_s - \frac{1}{2} \Gamma_c \chi_{RPA}^c(\mathbf{k} - \mathbf{k}', \omega) \Gamma_c + \frac{1}{2} \Gamma_c \right]_{cd}^{ab}, \quad (2)$$

where ω is a real frequency and $a, b, c,$ and d as before are orbital indices. In Eq. (2), the spin and charge vertices Γ_s and Γ_c are $\Gamma_s^{\tau\tau, \tau\tau} = U$, $\Gamma_s^{\tau\tau', \tau\tau'} = U'$, $\Gamma_s^{\tau\tau, \tau'\tau'} = J_H$, $\Gamma_s^{\tau\tau', \tau'\tau} = J_C$, and $\Gamma_c^{\tau\tau, \tau\tau} = U$, $\Gamma_c^{\tau\tau', \tau'\tau} = -U' + 2J_H$, $\Gamma_c^{\tau\tau, \tau'\tau'} = 2U' - J_H$, $\Gamma_c^{\tau\tau', \tau'\tau} = J_C$, where non-vanishing vertices are only between the same Fe, and τ labels orbitals and $\tau \neq \tau'$. In the following, we will take the relations $U' = U - 2J_H$ and $J_C = J_H$. The random phase approximation (RPA) for spin and charge susceptibilities are given by

$$\chi_{RPA}^s(\mathbf{q}, \omega) = \chi_0(\mathbf{q}, \omega) [1 - \Gamma_s \chi_0(\mathbf{q}, \omega)]^{-1}, \quad (3)$$

$$\chi_{RPA}^c(\mathbf{q}, \omega) = \chi_0(\mathbf{q}, \omega) [1 + \Gamma_c \chi_0(\mathbf{q}, \omega)]^{-1}, \quad (4)$$

with the bare susceptibility being given as

$$[\chi_0(\mathbf{q}, \omega)]_{ab}^{cd} = -\frac{1}{N} \sum_{\mathbf{k}, \mu, \nu} A_{c\mu}(\mathbf{k}) A_{a\mu}^*(\mathbf{k}) A_{b\nu}(\mathbf{k} + \mathbf{q}) A_{d\nu}^*(\mathbf{k} + \mathbf{q}) \times \frac{n_F[E_\mu(\mathbf{k})] - n_F[E_\nu(\mathbf{k} + \mathbf{q})]}{\omega + E_\mu(\mathbf{k}) - E_\nu(\mathbf{k} + \mathbf{q}) + i\delta}, \quad (5)$$

where $A_{a\mu}$ is the orbital-band transformation matrix from $\psi_a(\mathbf{k}) = \sum_\mu A_{a\mu}(\mathbf{k}) \gamma_\mu(\mathbf{k})$ and n_F is the Fermi-Dirac distribution function. In this work, we shall set the temperature to zero. Here $\chi_0(\mathbf{q}, \omega)$ is calculated by using the bare Green's function not the dressed one. The low energy physics of the scattering matrix is projected to scattering among the FS sheets. We shall denote the scattering matrix with a Cooper pair from $(\mathbf{k}', -\mathbf{k}')$ on FS- ν scattered to $(\mathbf{k}, -\mathbf{k})$ on FS- μ by $\tilde{\Gamma}_{\mu\nu}(\mathbf{k}, \mathbf{k}')$ ⁴⁴,

$$\tilde{\Gamma}_{\mu\nu}(\mathbf{k}, \mathbf{k}') = \Re \left\{ \sum_{a,b,c,d} A_{a\mu}^*(\mathbf{k}) A_{d\mu}^*(-\mathbf{k}) \times \Gamma_{cd}^{ab}(\mathbf{k}, \mathbf{k}'; 0) A_{b\nu}(\mathbf{k}') A_{c\nu}(-\mathbf{k}') \right\}. \quad (6)$$

Since we consider the even-parity pairing, we shall symmetrize the scattering matrix as $\tilde{\Gamma}_{\mu\nu}^{even}(\mathbf{k}, \mathbf{k}') = \frac{1}{2} [\tilde{\Gamma}_{\mu\nu}(\mathbf{k}, \mathbf{k}') + \tilde{\Gamma}_{\mu\nu}(\mathbf{k}, -\mathbf{k}')] .$

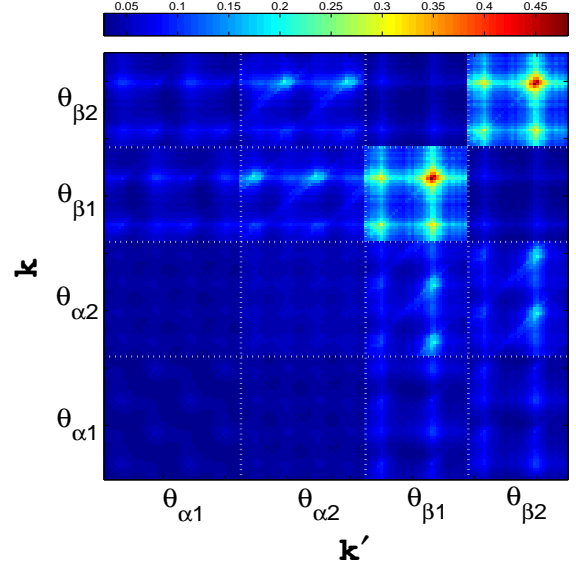


FIG. 2: (Color online) The weighted scattering matrix $[v_F(\mathbf{k})v_F(\mathbf{k}')]^{-1} \tilde{\Gamma}_{\mu\nu}^{even}(\mathbf{k}, \mathbf{k}')$ for \mathbf{k}, \mathbf{k}' being parameterized by $\theta_{\alpha 1}, \theta_{\alpha 2}, \theta_{\beta 1},$ and $\theta_{\beta 2}$ as defined in Fig. 1. Here the dotted white lines separate different FS sheets. Values of θ range from 0° to 360° in each block bounded by dotted white lines, which represents the change of angles of \mathbf{k} as it moves around the corresponding Fermi surfaces. Values of parameters are set with $U=1.0\text{eV}$ and $J_H=0.2U$.

For a given gap function $g(\mathbf{k})$, a dimensionless coupling constant is defined by⁴⁶

$$\lambda = \frac{-\frac{1}{N_p} \sum_{\mu, \nu} \sum_{\mathbf{k}, \mathbf{k}'} \frac{1}{v_F(\mathbf{k})v_F(\mathbf{k}')} g(\mathbf{k}) \tilde{\Gamma}_{\mu\nu}^{even}(\mathbf{k}, \mathbf{k}') g(\mathbf{k}')}{\sum_{\mu} \sum_{\mathbf{k}} \frac{1}{v_F(\mathbf{k})} g^2(\mathbf{k})}. \quad (7)$$

Here \mathbf{k} and \mathbf{k}' are restricted within FS μ and ν , respectively. $v_F(\mathbf{k}) = |\nabla_{\mathbf{k}} E_\mu(\mathbf{k})|$ is the Fermi velocity, and $N_p (=216)$ is the number of \mathbf{k} on Fermi surfaces we choose. The coupling constant includes contributions from pocket-pocket scattering processes, and it is helpful to extract them and to denote by a matrix $(\hat{\lambda})_{\mu\nu}$, satisfying $\lambda = \sum_{\mu, \nu} (\hat{\lambda})_{\mu\nu}$, where μ, ν refer to FS sheets, $\mu, \nu=1$ to $\alpha_1, 2$ to $\alpha_2, 3$ to $\beta_1,$ and 4 to β_4 .

The stationary condition in Eq. (7) $(\delta\lambda [g(\mathbf{k})] / \delta g(\mathbf{k}) = 0)$ leads to the eigenvalue problem

$$-\frac{1}{N_p} \sum_{\mathbf{k}'} \frac{1}{v_F(\mathbf{k}')} \tilde{\Gamma}_{\mu\nu}^{even}(\mathbf{k}, \mathbf{k}') g_a(\mathbf{k}') = \lambda_a g_a(\mathbf{k}), \quad (8)$$

where the subscript a stands for different solutions. For a given eigenvalue λ_a , its eigenfunction $g_a(\mathbf{k})$ determines the symmetry of the gap, which could be s -wave or d -wave. An s -wave state is characterized by $g_a(\mathbf{k}) = g_a(\mathcal{R}\mathbf{k})$ and d -wave by $g_a(\mathbf{k}) = -g_a(\mathcal{R}\mathbf{k})$, where \mathcal{R} is the 90° -rotational operation on \mathbf{k} . Among the s -wave

solutions, we pick up the largest one and set it to be λ_s and its eigenfunction to be g_s . Similarly, for the d -wave, they are denoted by λ_d and g_d . The eigenvalue equation Eq. (7) is not identical to the Bethe-Salpeter equation in which magnitude of unity for the eigenvalue stands for the formation of superconductivity. Instead, eigenvalues in Eq. (7) stand for the pairing strength. Therefore, the SC state is determined by largest one of λ_s and λ_d .

III. NUMERICAL RESULTS

A. Scattering Matrix

The scattering matrix shows some clues to the gap function. In order to gain more condensation energy, the gap should be larger in the region where the scattering matrix is maximal in magnitude. As the interaction is repulsive, the gap becomes anisotropic and sign-changing. Fig. 2 shows the "weighted" scattering matrix $[v_F(\mathbf{k})v_F(\mathbf{k}')]^{-1}\tilde{\Gamma}_{\mu\nu}^{even}(\mathbf{k},\mathbf{k}')$ for $U=1.0\text{eV}$ and $J_H=0.2U$. Here because the inverse Fermi velocity (IFV), $1/v_F(\mathbf{k})$, is related to the density of states (DOS), it is used as a weighting factor at each point. The scattering matrix contains intra and inter pocket scattering channels and different pockets are discriminated by the white dotted lines. The angles, θ_{α_1} , θ_{α_2} , θ_{β_1} and θ_{β_2} parameterizing momenta \mathbf{k} (\mathbf{k}'), increase from 0° to 360° as the coordinate increases from the bottom (left) to the top (right). Although we only show the result from one of the electron pocket β_1 (β_2), due to the nature of being even parity for $\tilde{\Gamma}_{\mu\nu}^{even}(\mathbf{k},\mathbf{k}')$, the result at the inversion point can be deduced.

In Fig. 2, the intra-electron-pocket (β_1 - β_1 or β_2 - β_2) scattering is much stronger than other channels and gives peaks at two momenta, $\theta_{\beta_1} \approx 48^\circ$ and 225° as the antipodes (on the major axis) of the electron pockets. The strong intensity of the scattering matrix at these two momenta is expected because large IFV happens about the antipodes of the elliptic FS ($1/v_F(\mathbf{k})$ is shown in Fig. 6). One of the reasons why intra-electron-pocket scattering is strong is due to the much larger DOS on the electron pockets. This also explains why the inter-electron-hole-pocket scattering is stronger than the intra- and the inter-hole-pocket scattering. Furthermore, the intra-electron-pocket scattering comes from exchange of fluctuations at vectors $\mathbf{q} \approx (0,0)$ and (π,π) , and the latter is driven by the substantial checkerboard antiferromagnetic fluctuations. The strength of DOS, however, can not explain why the inter-electron-pocket (β_1 - β_2) scattering is much small because the stripe antiferromagnetic fluctuations at $\mathbf{q} = (\pi,0)$ are not weak at all. A detailed analysis shows that the reduction of the inter-electron-pocket scattering is due to the difference in the orbital-band matrix element. In Fig. 3, we show the orbital weight $|A_{a\mu}(\mathbf{k})|^2$ for every FS sheet. Here lines represent Fe-A/C and legends with circles and triangles represent Fe-B/D. Note that different curves exhibited

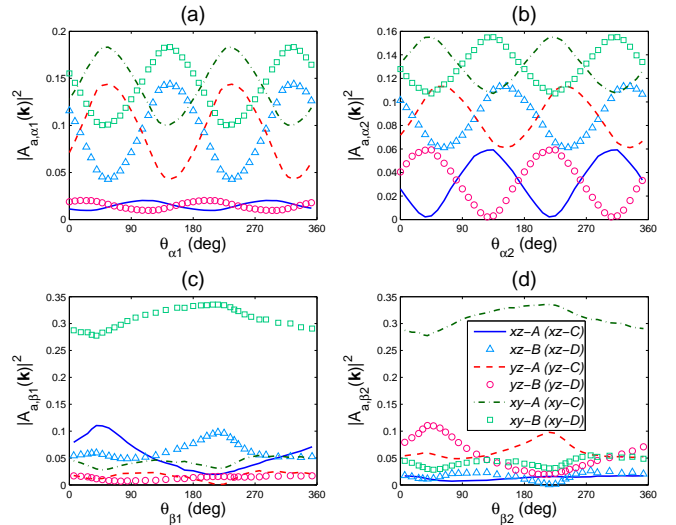


FIG. 3: (Color online) Orbital weight $|A_{a\mu}(\mathbf{k})|^2$ around FS sheets, $\mu = \alpha_1$ (a), α_2 (b), β_1 (c), and β_2 (d). Here lines (solid, dashed, and dash-dotted) represent Fe-A/C and legends (triangular, circular, and square) represent Fe-B/D. Different curves are related by rotational symmetry (see text).

in Fig.3 are related by rotational symmetry⁴¹. For example, a 90° rotation about the center of the unit cell located at the position of Se changes Fe-A to Fe-B and d_{xz} to d_{yz} . As a result, as shown in Figs. 3(a) or 3(b), weight curve of orbital-(yz, B) is equal to that of orbital-(xz, A) shifted by a phase $\pi/2$. Similarly, since orbital-(xz, C) can be obtained by a 180° rotation of orbital-(xz, A), they have the same weight too. This is the relation within the Fermi surface of α_1 or α_2 . For relations between different Fermi surfaces, since the same rotation changes FS- β_1 to FS- β_2 and relevant orbits also change under the rotation, the orbital components on different FS- β would be highly different. For instance, in Figs. 3(c) and 3(d), the major component on FS- β_1 is orbital-(xy, B), while it is (xy, A) on FS- β_2 and weights of other orbits are much smaller. Because vertices in the fluctuation exchange formula in Eq. (2) only couple orbitals on the same Fe, the inter-electron-pocket scattering will be heavily reduced. We have examined the case of neglecting the orbital-band matrix elements in Eq. (6) by setting $A_{a\mu}(\mathbf{k}) = 1/\sqrt{12}$ and find that the inter-electron-pocket scattering becomes comparable to the intra-electron-pocket one. Therefore, the small inter-electron-pocket scattering is due to the small magnitude of the orbital-band matrix element.

B. Phase Diagram of Superconductivity

After a better understanding of the scattering matrix, we now show the results of eigenvalues from the eigen-

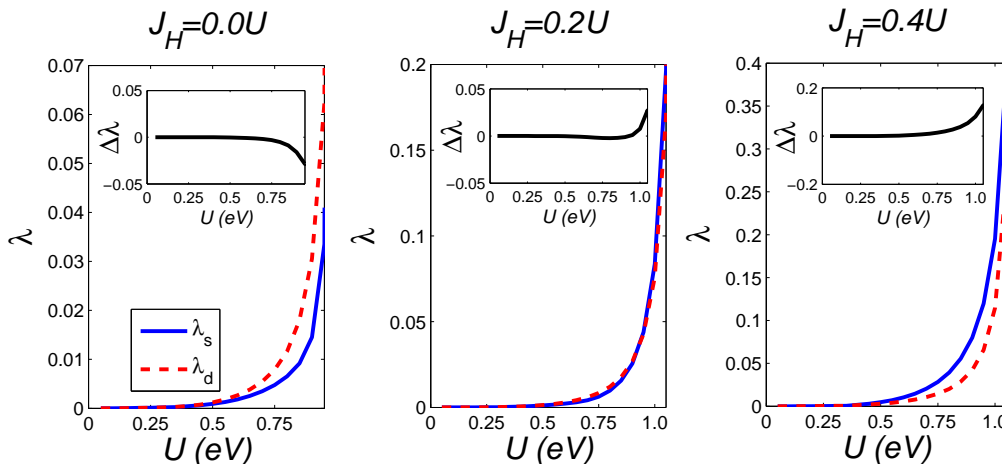


FIG. 4: (Color online) Eigenvalues or dimensionless coupling constants λ_s (s -wave) and λ_d (d -wave) as functions of U for $J_H=0, 0.2U$, and $0.4U$ from the left panel to the right one. Solid lines are for λ_s and dashed lines are for λ_d . Insets are the difference of eigenvalues, $\Delta\lambda = \lambda_s - \lambda_d$, to exhibit the favorable state. The eigenvalues for $J_H=0$ are smaller, but they grow up fast and solutions become unstable at about $U=1.0\text{eV}$.

value problem in Eq. (8). Fig. 4 displays the largest eigenvalues of s -wave (λ_s) and d -wave (λ_d) as functions of U in three Hund's rule couplings, $J_H=0, 0.2U$ and $0.4U$. λ_s is represented by solid blue lines while λ_d is represented by dashed red ones. As the interaction U is increased, quantum fluctuations enhances the SC pairing and then λ 's increase. Moreover, we observe that at different J_H , the dimensionless coupling constants for different symmetry grow in different speeds. As shown in the insets where the differences of two eigenvalues $\Delta\lambda \equiv \lambda_s - \lambda_d$ are plotted, the d -wave is always more stable against the s -wave ($\Delta\lambda < 0$) at $J_H=0$, while the preference is reverse ($\Delta\lambda > 0$) at $J_H=0.4U$. Between them at $J_H=0.2U$, the d -wave is favored for $U \lesssim 1.0\text{eV}$ but becomes unfavorable above that.

The above results indicate that the Hund's rule coupling is a parameter of controlling the SC symmetry as well as the AFM order⁴¹. This is further supported by Fig. 5, in which $\Delta\lambda$ versus J_H at different U is plotted. Except for the small phase space with $U=1.0\text{eV}$ and $J_H < 0.4U$, $\Delta\lambda$ increases monotonously with J_H , indicating that the Hund's rule coupling favors the s -wave. However, $\Delta\lambda$ is not a monotonic function of U . There exists a critical J_H , $J_{H,c} \approx 0.2U$, separating two states; below it, $\Delta\lambda$ decreases as U increases, but above it, $\Delta\lambda$ increases with U . Unless further symmetry is broken, s -wave and d -wave do not mix and the phase transition between them is first order.

C. Gap Functions

With the phase diagram of superconductivity, one still needs to know the gap function explicitly to understand its physics, especially in this new type of system with space group different from other iron-based superconduc-

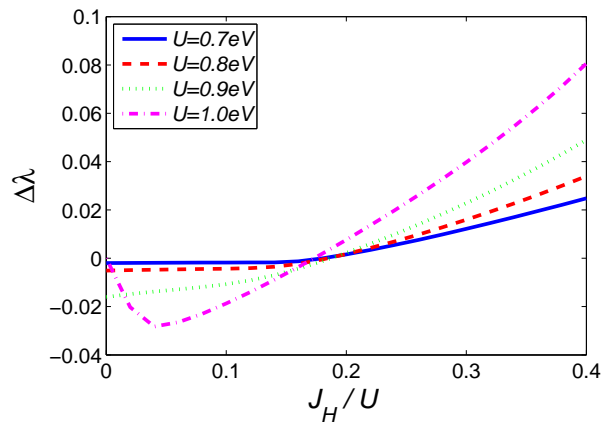


FIG. 5: (Color online) The eigenvalue differences between the s -wave and the d -wave, $\Delta\lambda$, as functions J_H/U in four cases of U : $U=0.7\text{eV}$ (solid line), $U=0.8\text{eV}$ (dash line), $U=0.9\text{eV}$ (dotted line), and $U=1.0\text{eV}$ (dash-dotted line). A critical J_H ($\approx 0.2U$) is observed as the transition point between s -wave and d -wave.

tors. We shall first examine the case of s -wave solution in Fig. 6 and then the d -wave one in Fig. 7.

1. s -wave

Following Ref.[6], we shall speak of s -wave by $g_a(\mathcal{R}\mathbf{k}) = g_a(\mathbf{k})$ with \mathcal{R} being the 90° -rotational operation on \mathbf{k} . Fig. 6 shows the s -wave gap function $g_s(\mathbf{k})$ along FS sheets α_1 , α_2 , and β_1 for $U=1.0\text{eV}$ and $J_H=0.2U$. $g_s(\mathbf{k})$ on FS- β_2 not shown is the same as on FS- β_1 when $\theta_{\beta_2} = \theta_{\beta_1}$. Blue squares are the eigenvalue-

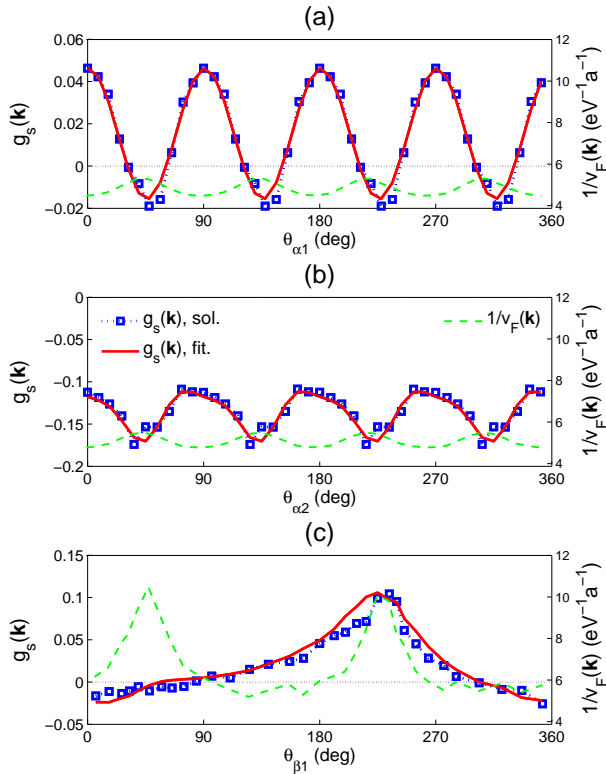


FIG. 6: (Color online) s -wave eigenfunction $g_s(\mathbf{k})$ for $U=1.0\text{eV}$ and $J_H=0.2U$. Panel (a) is along FS- α_1 , (b) along FS- α_2 , and (c) along FS- β_1 . Squares represent the eigenvalue-problem solution and the solid lines are the fitting curves using function forms shown in the text. Due to the s -wave character, the gap function on FS- β_1 and FS- β_2 is related by $g_s(\theta_{\beta_2}) = g_s(\theta_{\beta_1})$ when $\theta_{\beta_2} = \theta_{\beta_1}$. The factor, $1/v_F(\mathbf{k})$, being proportional to DOS, is also shown by the dashed green lines. a is the lattice length and its value from transmission electron microscopy⁴⁷ is about 6.15\AA .

problem solution, while the solid red lines are the fit guided by eye. One of the features is that such defined s -wave gap have multi-nodes on FS- α_1 , β_1 and β_2 . Moreover, because there is no reflection symmetry, there is an extra degree of freedom in defining origins of angles. As a result, the fitting curves for s -wave symmetry, chosen from lowest harmonic functions, are found to be

$$\begin{aligned}
 g_s(\theta_{\alpha_1}) &= 0.031 \cos[4(\theta_{\alpha_1} - 1^\circ)] + 0.0153, \\
 g_s(\theta_{\alpha_2}) &= 0.028 \cos[4(\theta_{\alpha_2} + 5^\circ)] \\
 &\quad + 0.008 \cos[8(\theta_{\alpha_2} - 22^\circ)] - 0.136, \\
 g_s(\theta_{\beta_1}) &= 0.13 [\cos(k'_x) + \cos(k'_y)] \\
 &\quad + 0.28 \cos(k''_x) \cos(k''_y) - 0.03, \quad (9)
 \end{aligned}$$

where $k'_x = k_x \cos(32^\circ) - k_y \sin(32^\circ)$, $k'_y = k_x \sin(32^\circ) + k_y \cos(32^\circ)$ and $k''_x = k_x \cos(4^\circ) + k_y \sin(4^\circ)$, $k''_y = -k_x \sin(4^\circ) + k_y \cos(4^\circ)$. Here $\cos 4\theta$, $\cos 8\theta$, $\cos(k_x) +$

$\cos(k_y)$, and $\cos(k_x) \cos(k_y)$ are the common s -wave bases. (Because FS- β_1 is not located on symmetric point, a different type of bases is adopted.) However, due to broken reflection symmetry, origins of angles get shifted by 1° , -5° , 22° and 20° . These angles are the allowed degrees of freedom in the C_{4h} symmetry and their precise values are to minimize the total energy of the system.

Similar to the s^\pm -wave proposed in iron-pnictide superconductor⁴⁸, where the SC order parameter on hole pockets and on electron pockets have opposite signs to make superconductivity stable, here we have the similar mechanism. In Fig. 6, we see that the mean value of the gap on FS- α_2 has an opposite sign to those on FS- α_1 and FS- β 's, which suggests these inter-pocket scatterings gain energy. Due to their larger scattering strength, the $\alpha_2 - \beta$'s scattering processes gain most energy. The $\alpha_1 - \beta$'s scattering processes are not favorable due to large cancellation by the oscillating behavior between positive and negative of gap on FS- α_1 . For the intra-pocket scattering processes, because the Fermi surfaces are small and if the fluctuations are smooth over the wave vector \mathbf{k} , the interaction would not able to change from repulsive to attractive. However, the repulsive strength can be reduced by making the gap oscillatory and even with the sign being changed. The reason why gap functions take the particular forms of Eq. (9) can be traced back to the behavior of the inverse Fermi velocity (IFV), which is shown as the dashed lines in Fig. 6. Clearly, the oscillatory behavior of gap functions results from oscillatory IFV. On FS- β_1 , the IFV is peaked at $\theta_{\beta_1} \approx 225^\circ$ where the gap is a peak too. The fact that the other point at $\theta_{\beta_1} \approx 48^\circ$ with high IFV does not lead to a large gap is because the repulsion can be lowered in the intra- and inter-electron-pocket scattering processes. Due to that gap functions on FS- β change slowly, it is clear that when the gap on FS- α_2 is in-phase with IFV and does not change sign, one gains energy in $\alpha_2 - \beta$'s scatterings but loses energy in the intra-pocket scatterings. The compromise between the intra- and inter-pocket scattering processes results in the gap function on FS- α_1 with the gap function being about $\frac{\pi}{2}$ out of phase relative to IFV. In the following, we list numerical values of the coupling matrix $\hat{\lambda}_s/\lambda_s$, which are consistent with the above explanations:

$$\frac{\hat{\lambda}_s}{\lambda_s} = \begin{bmatrix} -0.0275 & 0.2628 & -0.1039 & -0.1039 \\ & -2.8292 & 1.6033 & 1.6033 \\ & & -1.1398 & -0.1947 \\ & & & -1.1398 \end{bmatrix},$$

where due to that $\hat{\lambda}_s$ is a symmetric matrix, the lower-triangular matrix elements are omitted for brevity, and $\lambda_s = \sum_{\mu,\nu} (\hat{\lambda}_s)_{\mu\nu} = 0.0837$.

2. d -wave

Similar to the s -wave, the d -wave that we shall speak of obeys $g_a(\mathcal{R}\mathbf{k}) = -g_a(\mathbf{k})$ with \mathcal{R} being the 90° -rotational

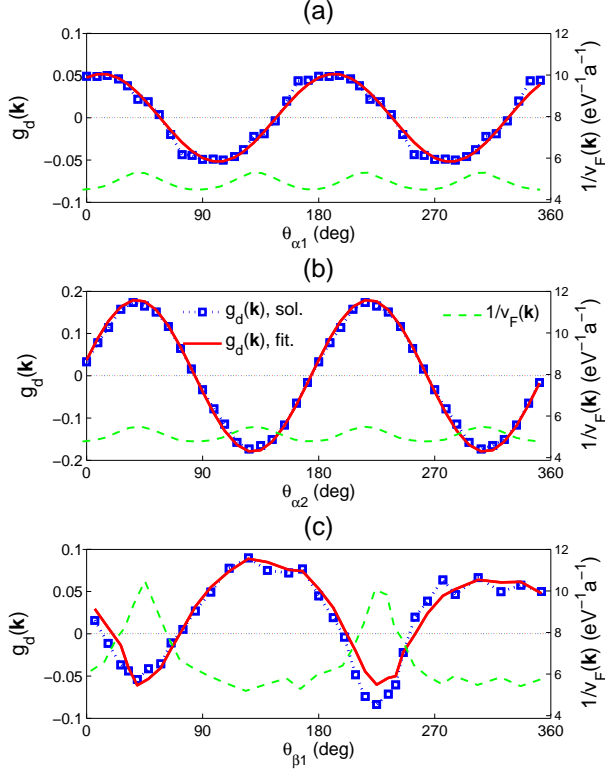


FIG. 7: (Color online) d -wave eigenfunction $g_d(\mathbf{k})$ for $U=0.9\text{eV}$ and $J_H=0.0$. Due to the d -wave character, $g_d(\theta_{\beta 2}) = -g_d(\theta_{\beta 1})$ when $\theta_{\beta 2} = \theta_{\beta 1}$. Here legends represent the same meaning as those in Fig. 6 while the fitting curves are different and are discussed in the text.

operation on \mathbf{k} . In Fig. 7, we show the d -wave gap function $g_d(\mathbf{k})$ for $U=0.9\text{eV}$ and $J_H=0$. $g_d(\mathbf{k})$ on FS- β_1 and on FS- β_2 is equal in magnitude but has opposite signs, *i.e.*, $g_d(\theta_{\beta 2}) = -g_d(\theta_{\beta 1})$ when $\theta_{\beta 2} = \theta_{\beta 1}$. It is seen that the gap function of d -wave always exhibits nodes on any Fermi surface. The fitted functions in Fig. 7 (solid red) are given by

$$\begin{aligned} g_d(\theta_{\alpha 1}) &= 0.052 \cos[2(\theta_{\alpha 1} - 12^\circ)], \\ g_d(\theta_{\alpha 2}) &= 0.18 \cos[2(\theta_{\alpha 2} - 39^\circ)], \\ g_d(\theta_{\beta 1}) &= 0.04 [\cos(k'_x) - \cos(k'_y)] \\ &\quad - 0.3 \sin(2k''_x) \sin(2k''_y), \end{aligned} \quad (10)$$

where $k'_x = k_x \cos(20^\circ) - k_y \sin(20^\circ)$, $k'_y = k_x \sin(20^\circ) + k_y \cos(20^\circ)$, $k''_x = k_x \cos(2^\circ) + k_y \sin(2^\circ)$, and $k''_y = -k_x \sin(2^\circ) + k_y \cos(2^\circ)$. Note that instead of $\cos 4\theta$ (which is correct for the s -wave), d -wave is represented by $\cos 2\theta$. Similar to the s -wave case, although nodes appear on every FS sheet, they are shifted away from the diagonal directions.

The main cause for the occurrence of d -wave differs from that for the s -wave and is primarily due to reduc-

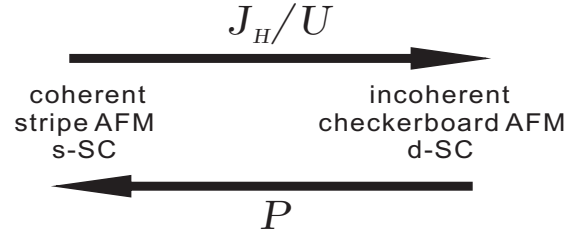


FIG. 8: Phase tendency of iron-vacancy-ordered $\text{A}_y\text{Fe}_{2-x}\text{Se}_2$ versus the Hund's rule coupling over the Hubbard U (J_H/U) and the pressure (P). Here arrows point to the direction that the corresponding parameters increase their strength. Since increase of the pressure generally reduces J_H/U (see text), the increase of J_H/U or the decrease of P would drive the multi-orbital electronic system from coherent to incoherent, or from stripe to checkerboard AFM state, or from d -wave to s -wave SC state found in this work.

tion of repulsion in intra-pocket and inter-electron-pocket scatterings through its sign-changing character. As a result, both antipodes on FS- β_1 ($\theta_{\beta 1} \approx 48^\circ$ and 225°) have large gaps in Fig. 7, in comparison to a single hump of the s -wave in Fig. 6. The coupling constant matrix $(\hat{\lambda}_d)_{\mu\nu}$ summarizes the above effects

$$\frac{\hat{\lambda}_d}{\lambda_d} = \begin{bmatrix} 0.0033 & 0.0361 & 0.0066 & 0.0066 \\ & -0.0393 & 0.2623 & 0.2623 \\ & & -0.0459 & -0.0066 \\ & & & -0.0459 \end{bmatrix},$$

where $\lambda_d = \sum_{\mu,\nu} (\hat{\lambda}_d)_{\mu\nu} = 0.0305$. Note that not only the repulsion between intra-pocket electrons is reduced, due to the presence of nodes, the attraction between inter-pocket electrons is also reduced. Although the d -wave state might not gain much energy from inter-pocket scattering processes relative to the s -wave state, it saves more energy from the reduction of intra-pocket repulsion.

IV. SUMMARY

Proximity of antiferromagnetism and superconductivity in $\text{A}_y\text{Fe}_{1.6}\text{Se}_2$ implies that the SC state could be derived from spin fluctuations. Under this assumption and assuming that superconductivity exists in the $\sqrt{5} \times \sqrt{5}$ iron-vacancy ordering state, we study the SC states from the effective pairing interaction in the FLEX approximation based on our previous 12-orbital tight-binding model⁴¹. Similar to that of iron-pnictide superconductors, for the spin-singlet superconductivity, s -wave and d -wave states are found to be close in energy. In particular, a quantum critical point is found at $J_H \approx 0.2U$, below which the d -wave prevails, while above which the s -wave wins over. Furthermore, unlike the iron-pnictide superconductors, the iron-vacancy order lowers the symmetry to the group C_{4h} so that the gap functions do not

need to be reflection symmetric. Therefore, symmetric axes of the pairing momenta do not need to coincide with axes of the unit cell. As a result, the relative orientations of the pairing wave functions to the lattice, i.e., origins of angles for the pairing momenta, become new degrees of freedom for characterizing the superconducting gaps. This implies that the complete order parameters for characterizing the superconductivity in $A_y\text{Fe}_{1.6}\text{Se}_2$ consist of both the magnitude of the gap and the orientation of the pairing wave function relative to the underlying lattice.

Finally, while our work focuses on the superconductivity, the finding of quantum critical point controlled by J_H in superconductivity is not an accident. In the magnetism, we have shown that J_H controls the magnetic phase transition from the stripe to the checkerboard antiferromagnetism⁴¹. In addition, Haule and Kotliar⁴⁵ show that the crossover between coherence and incoherence is also determined by J_H . Therefore, the Hund's rule coupling plays the dominant role in determining localization, magnetism, and superconductivity of iron-based superconductors. Experimentally, it is observed that applying pressure drives the magnetic phase transition^{20,21} that accompanies the metal-

to-semiconductor transition. Although in general, applying pressure affects itinerary electrons and could change J_H and U , the experimental results, when combined with our results on magnetism⁴¹, indicate that increase of the pressure generally reduces J_H/U in this system. Therefore, the phase tendency for iron-vacancy-ordered $A_y\text{Fe}_{2-x}\text{Se}_2$ can be summarized in Fig.8. The tendency implies that by appropriately changing the applied pressure, transition between different pairing symmetry of superconductivity can be induced. While the phase tendency shown in Fig. 8 needs further supports from experimental confirmation, our results provide a useful guide in clarifying the origin of unconventional superconducting gaps and searching for a possible quantum phase transition in iron-vacancy-ordered $A_y\text{Fe}_{2-x}\text{Se}_2$.

Acknowledgments

We thank Dr. Ming-Chang Chung for useful discussions. This work was supported by the National Science Council of Taiwan.

-
- ¹ G. R. Stewart, *Rev. Mod. Phys.* **83**, 1589 (2011).
² H. Oh, J. Moon, D. Shin, C.-Y. Moon, and H. J. Choi, *Progress in Superconductivity* **13**, 65-84 (2011).
³ K. Kuroki, S. Onari, R. Arita, H. Usui, Y. Tanaka, H. Kontani, and H. Aoki, *Phys. Rev. Lett.* **101**, 087004 (2008).
⁴ I.I. Mazin and J. Schmalian, *Physica C* **469**, 614 (2009).
⁵ H. Zhai, F. Wang, and D.-H. Lee, *Phys. Rev. B* **80**, 064517 (2009).
⁶ S. Graser, T. A. Maier, P. J. Hirschfeld, and D. J. Scalapino, *New J. Phys.* **11**, 025016 (2009).
⁷ J. Guo, S. Jin, G. Wang, S. Wang, K. Zhu, T. Zhou, M. He, and X. Chen, *Phys. Rev. B* **82**, 180520(R) (2010).
⁸ W. Bao, Q. Huang, G. F. Chen, M. A. Green, D. M. Wang, J. B. He, X. Q. Wang, and Y. Qiu, *Chin. Phys. Lett.* **28**, 086104 (2011).
⁹ J. Bacsá, A. Y. Ganin, Y. Takabayashi, K. E. Christensen, K. Prassides, M. J. Rosseinsky, and J. B. Claridge, *Chem. Sci.* **2**, 1054 (2011).
¹⁰ X.-W. Yan, M. Gao, Z.-Y. Lu, and T. Xiang, *Phys. Rev. B* **83**, 233205 (2011).
¹¹ M. H. Fang, H. D. Wang, C. H. Dong, Z. J. Li, C. M. Feng, J. Chen, and H. Q. Yuan, *Europhys. Lett.* **94**, 27009 (2011).
¹² D. M. Wang, J. B. He, T.-L. Xia, and G. F. Chen, *Phys. Rev. B* **83**, 132502 (2011).
¹³ Z. Wang, Y. J. Song, H. L. Shi, Z. W. Wang, Z. Chen, H. F. Tian, G. F. Chen, J. G. Guo, H. X. Yang, and J. Q. Li, *Phys. Rev. B* **83**, 140505(R) (2011).
¹⁴ B. Shen, B. Zeng, G. F. Chen, J. B. He, D. M. Wang, H. Yang, and H. H. Wen, *Europhys. Lett.* **96**, 37010 (2011).
¹⁵ D. H. Ryan, W. N. Rowan-Weetaluktuk, J. M. Cadogan, R. Hu, W. E. Straszheim, S. L. Bud'ko, and P. C. Canfield, *Phys. Rev. B* **83**, 104526 (2011).
¹⁶ F. Chen, M. Xu, Q. Q. Ge, Y. Zhang, Z. R. Ye, L. X. Yang, Juan Jiang, B. P. Xie, R. C. Che, M. Zhang, A. F. Wang, X. H. Chen, D. W. Shen, J. P. Hu, and D. L. Feng, *Phys. Rev. X* **1**, 021020 (2011).
¹⁷ A. Ricci, N. Poccia, G. Campi, B. Joseph, G. Arrighetti, L. Barba, M. Reynolds, M. Burghammer, H. Takeya, Y. Mizuguchi, Y. Takano, M. Colapietro, N. L. Saini, and A. Bianconi, *Phys. Rev. B* **84**, 060511(R) (2011).
¹⁸ R. H. Yuan, T. Dong, Y. J. Song, G. F. Chen, J. P. Hu, J. Q. Li, and N. L. Wang, *Scientific Reports* **2**, 221 (2012).
¹⁹ W. Li, H. Ding, P. Deng, K. Chang, C. Song, K. He, L. Wang, X. Ma, J. P. Hu, X. Chen, and Q. K. Xue, *Nature Phys.* **8**, 126 (2012).
²⁰ L. Chen, X. W. Yan, Z. Y. Lu, and T. Xiang, e-print arXiv:1109.3049 (unpublished).
²¹ J. Guo, X. Chen, C. Zhang, J. Guo, X. Chen, Q. Wu, D. Gu, P. Gao, X. Dai, L. Yang, H. K. Mao, L. Sun, and Z. Zhao, arXiv:1101.0092 (unpublished).
²² Y. Liu, Z. C. Li, W. P. Liu, G. Friemel, D. S. Inosov, R. E. Dinnebier, Z. J. Li, and C. T. Lin, e-print arXiv:1201.0902 (unpublished).
²³ W. Yu, L. Ma, J. B. He, D. M. Wang, T.-L. Xia, G. F. Chen, and W. Bao, *Phys. Rev. Lett.* **106**, 197001 (2011).
²⁴ D. A. Torchetti, M. Fu, D. C. Christensen, K. J. Nelson, T. Imai, H. C. Lei, and C. Petrovic, *Phys. Rev. B* **83**, 104508 (2011).
²⁵ L. Ma, G. F. Ji, J. Zhang, J. B. He, D. M. Wang, G. F. Chen, W. Bao, and W. Yu, *Phys. Rev. B* **83**, 174510 (2011).
²⁶ The relevant spin fluctuation in this system is the checkerboard AFM fluctuation at $\mathbf{q}=(\pi,\pi)$, which is not revealed in the Knight shift K , which is related to the spin susceptibility at $\mathbf{q}=0$. For $1/T_1T$ on Se or on the mono-valence element A which locates at the center of the iron square, the form factor⁶ and iron deficiencies would suppress the

- effect of the checkerboard AFM fluctuation.
- ²⁷ A. M. Zhang, J. H. Xiao, Y. S. Li, J. B. He, D. M. Wang, G. F. Chen, B. Normand, Q. M. Zhang, and T. Xiang, e-print arXiv:1106.2706 (unpublished).
- ²⁸ T. A. Maier, S. Graser, P. J. Hirschfeld, and D. J. Scalapino, *Phys. Rev. B* **83**, 100515(R) (2011).
- ²⁹ F. Wang, F. Yang, M. Gao, Z. Y. Lu, T. Xiang, and D. H. Lee, *Europhys. Lett.* **93**, 57003 (2011).
- ³⁰ Y. Zhou, D. H. Xu, F. C. Zhang, and W. Q. Chen, *Europhys. Lett.* **95**, 17003 (2011).
- ³¹ T. Das and A. V. Balatsky, *Phys. Rev. B* **84**, 014521 (2011).
- ³² I. I. Mazin, *Phys. Rev. B* **84**, 024529 (2011).
- ³³ C. Fang, Y. L. Wu, R. Thomale, B. A. Bernevig, and J. P. Hu, *Phys. Rev. X* **1**, 011009 (2011).
- ³⁴ I. R. Shein and A. L. Ivanovskii, e-print arXiv:1012.5164 (unpublished).
- ³⁵ C. Cao and J. Dai, *Chin. Phys. Lett.* **28**, 057402 (2011).
- ³⁶ C. Cao and J. Dai, *Phys. Rev. Lett.* **107**, 056401 (2011).
- ³⁷ Y. Zhang, L. X. Yang, M. Xu, Z. R. Ye, F. Chen, C. He, H. C. Xu, J. Jiang, B. P. Xie, J. J. Ying, X. F. Wang, X. H. Chen, J. P. Hu, M. Matsunami, S. Kimura, and D. L. Feng, *Nat. Mater.* **10**, 273 (2011).
- ³⁸ D. Mou, S. Liu, X. Jia, J. He, Y. Peng, L. Zhao, L. Yu, G. Liu, S. He, X. Dong, J. Zhang, H. Wang, C. Dong, M. Fang, X. Wang, Q. Peng, Z. Wang, S. Zhang, F. Yang, Z. Xu, C. Chen, and X. J. Zhou, *Phys. Rev. Lett.* **106**, 107001 (2011).
- ³⁹ T. Qian, X.-P. Wang, W.-C. Jin, P. Zhang, P. Richard, G. Xu, X. Dai, Z. Fang, J.-G. Guo, X.-L. Chen, and H. Ding, *Phys. Rev. Lett.* **106**, 187001 (2011).
- ⁴⁰ L. Zhao, D. Mou, S. Liu, X. Jia, J. He, Y. Peng, L. Yu, X. Liu, G. Liu, S. He, X. Dong, J. Zhang, J. B. He, D. M. Wang, G. F. Chen, J. G. Guo, X. L. Chen, X. Wang, Q. Peng, Z. Wang, S. Zhang, F. Yang, Z. Xu, C. Chen, and X. J. Zhou, *Phys. Rev. B* **83**, 140508(R) (2011).
- ⁴¹ S. M. Huang and C. Y. Mou, *Phys. Rev. B* **84**, 184521 (2011).
- ⁴² N. E. Bickers, D. J. Scalapino, and S. R. White, *Phys. Rev. Lett.* **62**, 961 (1989).
- ⁴³ T. Takimoto, T. Hotta, and K. Ueda, *Phys. Rev. B* **69**, 104504 (2004).
- ⁴⁴ Similar to the electron-phonon case where the electron-phonon coupling constant is related to a frequency integral of the phonon density of states divided by frequency, the imaginary part of Γ_{cd}^{ab} plays the role of the phonon density of states in the fluctuation-exchange coupling. Therefore, the integral of $\Im\Gamma_{cd}^{ab}(\omega)/\omega$ will produce $\Re\Gamma_{cd}^{ab}(\omega = 0)$ by using the Kramers-Krönig relation⁶. Here the real part in Eq. (6) has taken account of the time reversal symmetry, $A_{a\mu}(-\mathbf{k}) = A_{a\mu}^*(\mathbf{k})$.
- ⁴⁵ K. Haule and G. Kotliar, *New J. Phys.* **11** 025021 (2009).
- ⁴⁶ D. Scalapino, E. Loh, and J. Hirsch, *Phys. Rev. B* **34**, 8190 (1986).
- ⁴⁷ Z. Wang, Y. J. Song, H. L. Shi, Z. W. Wang, Z. Chen, H. F. Tian, G. F. Chen, J. G. Guo, H. X. Yang, and J. Q. Li, *Phys. Rev. B* **83**, 140505(R) (2011).
- ⁴⁸ I. I. Mazin, D. J. Singh, M. D. Johannes, and M. H. Du, *Phys. Rev. Lett.* **101**, 057003 (2008).